






BASIC SCIENCE

Development of a microstructured tissue phantom with adaptable optical properties for use with microscopes and fluorescence lifetime imaging systems

Christian Freymüller M.Sc.^{1,2}  | Stephan Ströbl Dr. rer. biol. hum.^{1,2,3}  |
 Maximilian Aumiller M.Sc.^{1,2}  | Maximilian Eisel Dr. rer. biol. hum.^{1,2}  |
 Ronald Sroka Prof. Dr. rer. biol. hum.^{1,2}  | Adrian Rühm Dr. rer. nat.^{1,2}

¹Laser-Forschungslabor, LIFE Center, Department of Urology, University Hospital, LMU Munich, Munich, Germany

²Department of Urology, University Hospital, LMU Munich, Munich, Germany

³Research Center for Microtechnology, FH Vorarlberg, Dornbirn, Vorarlberg, Austria

Correspondence

Christian Freymüller, Laser-Forschungslabor, LIFE Center, Department of Urology, University Hospital, LMU Munich, Munich, Germany.

Email: Christian.Freymueller@med.uni-muenchen.de

Funding information

Bundesministerium für Bildung und Forschung, Grant/Award Number: 13N14507; Österreichische Forschungsförderungsgesellschaft, Grant/Award Number: 855657; Deutsche Forschungsgemeinschaft, Grant/Award Number: (RTG) GRK2274 Project number 299102935

Abstract

Objectives: For the development and validation of diagnostic procedures based on microscopic methods, knowledge about the imaging depth and achievable resolution in tissue is crucial. This poses the challenge to develop a microscopic artificial phantom focused on the microscopic instead of the macroscopic optical tissue characteristics.

Methods: As existing artificial tissue phantoms designed for image forming systems are primarily targeted at wide field applications, they are unsuited for reaching the formulated objective. Therefore, a microscopy- and microendoscopy-suited artificial tissue phantom was developed and characterized. It is based on a microstructured glass surface coated with fluorescent beads at known depths covered by a scattering agent with modifiable optical properties. The phantom was examined with different kinds of microscopy systems in order to characterize its quality and stability and to demonstrate its usefulness for instrument comparison, for example, regarding structural as well as fluorescence lifetime analysis.

Results: The analysis of the manufactured microstructured glass surfaces showed high regularity in their physical dimensions in accordance with the specifications. Measurements of the optical parameters of the scattering medium were consistent with simulations. The fluorescent beads coating proved to be stable for a respectable period of time (about a week). The developed artificial tissue phantom was successfully used to detect differences in image quality between a research microscope and an endoscopy based system. Plausible causes for the observed differences could be derived based on the well known microstructure of the phantom.

Conclusions: The artificial tissue phantom is well suited for the intended use with microscopic and microendoscopic systems. Due to its configurable design, it can be adapted to a wide range of applications. It is especially targeted at the characterization and calibration of clinical imaging systems that often lack extensive positioning capabilities such as an intrinsic z-stage.

KEYWORDS

artificial tissue phantom, endomicroscopy, endoscopy, fluorescence lifetime imaging, microscopy, two-photon fluorescence microscopy

Part of the inaugural thesis is to be submitted to the medical faculty of LMU Munich.

This is an open access article under the terms of the Creative Commons Attribution-NonCommercial-NoDerivs License, which permits use and distribution in any medium, provided the original work is properly cited, the use is non-commercial and no modifications or adaptations are made.

© 2022 The Authors. *Lasers in Surgery and Medicine* published by Wiley Periodicals LLC.

INTRODUCTION

Artificial tissue phantoms play an essential role in the development and validation of medical equipment.¹ Usually, artificial phantoms are designed to mimic only the macroscopic behaviour, i.e., spatially averaged properties of the biological tissue to be represented, for example, for a comparison of medical treatment methods.² This is useful if the system under development or investigation does not use image forming optics. For microscopy and microendoscopy, developing an equivalent artificial phantom is more demanding because of the requirement to implement and control small structures comparable to those of the biological tissue, and because of the related accuracy. For tissue diagnosis based on general microscopic methods, it is often necessary to know up to which depth meaningful images can be expected, that is, images in which structural features known to be present within the sample can still be visually distinguished. Such information is easy to obtain at a modern research microscope, since these microscopes are equipped with a motorized stage for precise movements in x , y and z -direction. Rather simple, that is, macroscopically homogeneous artificial tissue phantoms can be used in this case, such as an agar phantom with embedded scattering centres and fluorescent spheres,^{3,4} gold nano-rods,⁵ or a liquid phantom.⁶

In this case, the imaging depth, that is, the depth of the focal plane below the phantom surface, can simply be varied using the z -drive of the microscopy stage. In the case of endoscopic systems, both widefield or scanning type, the situation can be more difficult since they usually lack a positioning stage or provide only restricted positioning capabilities. In such cases^{7–11} and particularly in the case of fixed focus systems, the accessible depth range, the depth calibration, and the imaging quality in that range have to be assessed in a different way. Constructs designed for the evaluation of fluorescence cameras^{12,13} target these problems on a macroscopic scale, but they are not suited for scanning, especially depth-scanning microscopy, and microendoscopy systems. Tissue phantoms based on fluorophore- or blood-filled glass capillaries^{14,15} have been examined. These contain structures in the range of about $\approx 80\ \mu\text{m}$. Rather complex skin-mimicking phantoms¹⁶ contain artificial vessel structures in the range of 1 mm diameter. Publications about microstructured tissue phantoms containing finer structures are scarce. Phantoms published in literature are mostly based on stereolithography¹⁷ or two-photon polymerization,¹⁸ but still require a z -stage for depth determination or do not reach structure sizes as small as cellular dimensions.

This study presents an approach for the construction of microscopy- and microendoscopy-suited artificial tissue phantom with modifiable optical properties and fluorescent structures located at well-defined depths within a modifiable medium. This phantom is specifically designed to meet the technical need to characterize

clinical optical systems, which very often lack a z -stage. The phantom is based on a microstructured glass surface coated with fluorescent beads and covered with a scattering medium, consisting of non-fluorescent polystyrene beads in a hydrogel (Pluronic). The artificial tissue phantom was developed for the characterization of a microendoscopic multiphoton fluorescence lifetime microscopy (FLIM) systems for metabolic imaging, therefore it was adjusted to the spectral fluorescence excitation and emission characteristics of nicotinamide adenine dinucleotide (NADH) and flavin adenine dinucleotide (FAD). Fluorescent beads of $1\ \mu\text{m}$ diameter were chosen to mimic the size of mitochondria. Optical properties of the scattering medium were adjusted to human epithelial tissue in the upper respiratory tract. Despite this original design the artificial phantom can be adapted to a wide range of applications. Since fluorescent spheres are available for a multitude of spectral excitation and emission characteristics, and the scattering characteristics can be adapted as well, different kinds of biological tissue can be simulated.

Many imaging systems for clinical applications lack the extensive positioning capabilities known from modern research microscopes. To characterize these systems, there is need for a phantom with intrinsic lateral and axial position determination capability. The presented artificial tissue phantom is a step toward this direction. The aim of the development was to design a staircase-like phantom especially for mimicking features encountered when trying to optically diagnose the metabolic states of cells within the epithelial layers in the upper respiratory tract. This application may serve as an example for a variety of further applications.

MATERIAL AND METHODS

In the following sections “Glass structure” to “Scattering medium” the general design and the manufacturing methods of the artificial tissue phantom and applied characterization methods are described. In section “Simulated optical properties” the selection of phantom parameters is described. In section “Imaging” the image recording and analysis methods are described.

Glass structure

Standard microscopy slides (Superfrost PLUS, Art. no. J1800AMNZ, Gerhard Menzel GmbH) were used as substrate for the artificial phantoms. Into these slides, 65 steps of $5\ \mu\text{m}$ step height, $200\ \mu\text{m}$ tread length and 5 mm width were inscribed using a microstructuring laser system (microSTRUCTvario, 3D-Micromac AG) equipped with an ultrashort pulsed laser (Spirit HE 1040-30 SHG, SpectraPhysics) with emission wavelength 520 nm for material processing.

The script for creating the desired step structure was custom written and the machining pattern, number of passes as well as laser power were initially adjusted in order to produce surfaces as even as possible. Figure 1 shows a transmission image of a structured glass slide recorded with a flatbed scanner (CanoScan 8800F, Canon Inc.) and a magnified image recorded with a wide field microscope (DMIRBE, Leica Microsystems GmbH), equipped with a colour camera (DBK 38UX267, The Imaging Source), further referred to as wide-field microscope (WF-microscope). The size of these structures, centred on the slide in x - and y -direction, is specified in the figure. A simplified, not to scale, scheme of the described structure, with the fluorescent spheres coating and scattering medium indicated as described in sections “Fluorescent sphere coating” and “Scattering medium,” is shown in Figure 2.

A total of 10 structured slides were manufactured and individually characterized using a three-dimensional (3D) laser scanning microscope (VK-X260K, Keyence Corporation). Evaluation and visualization of the measurements was carried out with VK-X Series Software MultiFileAnalyzer (Version 1.3.1.34, Keyence Corporation), Gwyddion^{19,20} version 2.59 and Matlab (The Mathworks Inc.; Version 2018b).

The step heights and tread lengths of 10 manufactured step structures (referred to as St1–St10 in the following) were analysed based on the acquired 3D image stacks as follows. A depth profile $z_i(x_i)$, averaged over 50 adjacent y -planes, was extracted for each analysed structured slide along the x -axis using VK-X Series Software MultiFileAnalyzer (see Figure 3). Each profile was numerically differentiated using Matlab, which resulted in a series of peaks indicating the locations of the steps, that is, of the transitions between

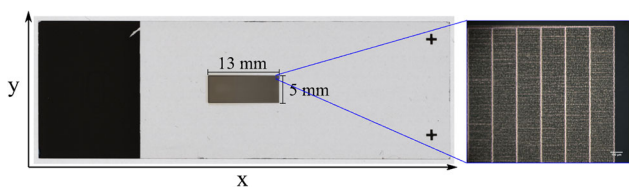


FIGURE 1 Sample image of an uncoated, unsealed, glass structure; standard microscopy slide, 76×26 mm, magnification of region within the small blue rectangle is shown in the right image: WF-microscope with objective PL Fluotar $\times 10/0.30$ PH 1 phase contrast, scale bar is $100 \mu\text{m}$.

adjacent treads. The corresponding peak positions \hat{x}_i were determined using Matlab's `findpeaks` function and the corresponding tread lengths L_i , Equation (1), calculated, taking into account the scanning resolution $\zeta = 0.697 \mu\text{m}$ of the microscope. The midpoint positions of the treads were defined in the centre between two adjacent step positions as \bar{x}_i , Equation (2). The depth positions \bar{z}_i of the treads were determined by averaging the profile $z_i(x_i)$ over $\pm 50 x_i$ positions around the x_i position closest to the midpoint position \bar{x}_i (corresponding to an average over 101 datapoints or $69.7 \mu\text{m}$). The step heights of the steps were then defined by the corresponding depth difference between the two adjacent treads as H_i , Equation (3), taking into account the z -resolution of the analysed image stack. The tread lengths and step heights of the examined structures were represented graphically and the mean and standard deviation calculated.

$$L_i = (\hat{x}_{i+1} - \hat{x}_i) \times \zeta \quad (1)$$

$$\bar{x}_i = \left\lfloor \frac{\hat{x}_i + \hat{x}_{i+1}}{2} \right\rfloor \quad (2)$$

$$H_i = \bar{z}_i - \bar{z}_{i-1} \quad (3)$$

Fluorescent sphere coating

The slides, like the one exemplary shown in Figure 1, were cleaned before each imaging using a lab washer (Miele Professional PG 8593) and coated with blue and yellow/green fluorescent beads of $1 \mu\text{m}$ diameter (FluoSpheres F8814 and FluoSpheres F8823, respectively, both Thermo Fisher Scientific). The beads were chosen to mimic the fluorescent properties of NADH and FAD since the phantom was designed for testing equipment for metabolic imaging. Figure 4 shows a comparison of the beads two-photon fluorescence spectra with that of NADH (N8129, Sigma-Alrch GmbH) and FAD (ALX-480-084-M050, Enzo Life Sciences GmbH) solutions in 7.5 pH TRIS buffer (BU-125S, TRIS 1 M pH 7.5 , Jena Bioscience GmbH). The two-photon spectra were recorded with a multiphoton FLIM microscope described previously.²¹

To fix the fluorescent beads on the steps, they are dispersed ($1 \mu\text{l}$ of each fluorescent beads suspension) in

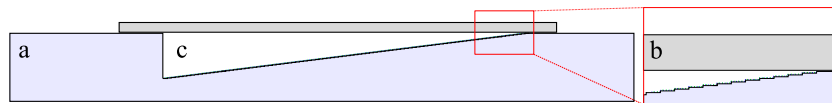


FIGURE 2 Simplified scheme of structure; (a) glass microscopy slide, (b) coverslip, and (c) pluronic solution (with or without scattering agent); image magnification (red); detailed view; the coating with fluorescent beads is indicated by blue and green dots on the horizontal planes of the step structure.

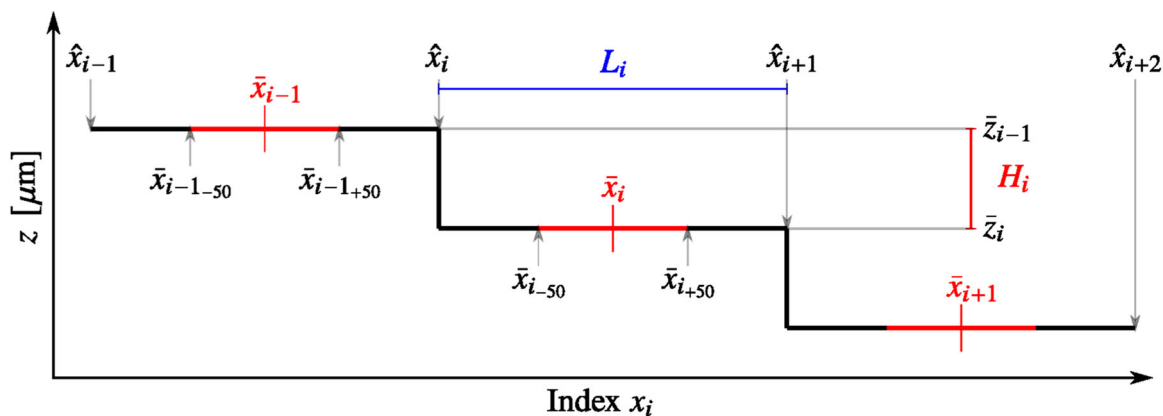


FIGURE 3 Scheme for calculating step length and step height of a step structure (not to scale).

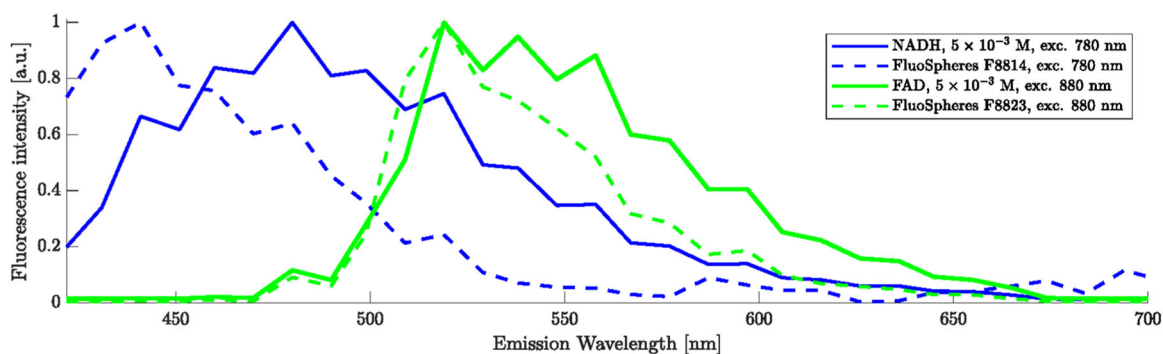


FIGURE 4 Comparison of the normalized two-photon fluorescence spectra of NADH, FAD, and blue and yellow/green fluorescent beads.

500 μl 0.9%w/w polyvinyl alcohol (PVA) solution (Art. no. 563900 Poly(vinyl alcohol), Sigma-Aldrich GmbH). Approximately 10 μl of the mixture is filled into the structures using a pipette, distributed to cover the whole structure and a small rim on the surface of the glass slide. The filled structure was then dried on a hot plate (RCT basic, IKA Labortechnik) at $\approx 60^\circ\text{C}$ and subsequently wrapped in aluminium foil for light protection until further use. The position of the fluorescent sphere coating is indicated by tiny blue and yellow dots in the scheme in Figure 2.

The adherence of the fluorescent bead coating was checked during imaging with a multiphoton microscope and in one case additionally, after 14 days storage, using a confocal microscope (TCS SP8 WLL AOBs with objective HC PL APO CS2 $\times 10/0.40$ DRY objective, both Leica Microsystems GmbH), further referred to as CF-microscope.

Scattering medium

To mimic light scattering in tissue, a scattering agent consisting of an aqueous 13%w/w Pluronic solution (Art. no. P2443, Sigma-Aldrich GmbH) and non-fluorescent

polystyrene beads of 1 μm diameter (Polybead Microspheres 1.00 μm , Cat. no. 07310-15, Polysciences Europe GmbH) was prepared and refrigerated until use. The scattering suspension was checked for homogeneity by visual inspection using the WF-microscope with objective HCX PL Fluotar $\times 20/0.50$ PH 2 (Leica Microsystems GmbH). Then ≈ 10 μl were filled in the indentation of the structure, which was then closed by a cover glass (VWR Cover Glass no. 1.5, Cat. no. 631-0136, VWR International GmbH) and sealed around the edges of the coverslip using a mounting medium (Eukitt 03989, Sigma-Aldrich GmbH). The position of the scattering medium in the glass structure is indicated as white area in the scheme in Figure 2.

For imaging with the FLIM platform (see chapter "Imaging" for description) the cover glass was substituted with cling film. This was necessary because the working distance of the custom made endoscope was between 25 and 100 μm , therefore a standard cover glass could not be used. Preliminary experiments with a multiphoton FLIM microscope (described in Freymüller et al.²¹) showed no significant reduction in image quality or introduction of detectable aberrations when a cling film was brought into the imaging path.

The concentrations of non-fluorescent polystyrene beads were adjusted, based on calculations of Mie

scattering taking the refractive index of the surrounding medium and the non-fluorescent beads into account, so as to mimic the scattering properties of a selected biological tissue (in this case oral mucosa). The Pluronic solution was modelled with a wavelength dependent refractive index identical to water^{22,23}, for the non-fluorescent beads the wavelength dependent refractive index of polystyrene^{24,25} was used. The reduced scattering coefficient μ'_s for a given mixing ratio of Polybead suspension and water/Pluronic solution was calculated based on Mie theory.²⁶ A customized Matlab algorithm based on literature^{27,28} was implemented for the Mie calculations and for the iterative determination of the mixing ratio required to obtain a given value of the reduced scattering coefficient μ'_s .

The resulting optical parameters were evaluated using an existing integrating sphere measurement setup described previously.²⁹ The setup, originally equipped with a white light source (DLight 201332 20, Karl Storz SE & Co. KG), was extended by integration of a 780 and 880 nm laser diode (LDM780/3LJ and LM-104-E002, respectively, both Roithner Lasertechnik GmbH). Polarization effects were not taken into account as they were supposed to be negligible due to multiple scattering events within the scattering medium.³⁰

The degradation of one artificial tissue phantom over the time course of 7 days was assessed by imaging with the transmitted light detector (TLD) of the CF-microscope at three different points in time: immediately (i.e., within 2 h) after preparation and after keeping it 3 and 7 days at room temperature ($\approx 20^\circ\text{C}$), wrapped in aluminium foil for light-protection. Degradation was defined qualitatively as any visible change in the phantom over time in comparison to the state immediately after preparation, as revealed under a microscope. This especially refers to aggregation/clotting or sedimentation of spheres in the scattering medium, detachment of the fluorescent spheres, or an eventual growth of bacteria or mold.

Simulated optical properties

In this section, the optical phantom parameters realized with the methods described in sections “Fluorescent sphere coating” and “Scattering medium” are specified. The aim pursued with the proposed artificial phantoms is to provide a well-defined, repeatable construct for acquiring optical resolution data dependent on the depth of the observed structure in the phantom. An important field of application is metabolic imaging by means of multiphoton FLIM. Therefore, the study was focused on two-photon excitation using wavelength between 700 and 900 nm, specifically 780 and 880 nm, and an emission wavelength range of 400–600 nm, as this corresponds well to the fluorescence characteristics of NADH and

FAD, the most important fluorophores for the investigation of cell metabolism. An ideal artificial tissue phantom would have two-photon excitation spectra and corresponding emission spectra exactly matching those of real biological cells or tissue, even in mixtures representing situations with coexisting cells in different states. This is practically impossible to achieve, even more in mixtures where different absorption and scattering agents may affect or interfere with each other. Since an artificial phantom has to be similar, but not identical¹ to what is simulated, the focus was primarily on the excitation wavelengths. Here the choice of excitation wavelength was motivated by existing two-photon FLIM microscopy systems to be examined and compared. In all cases, NADH, FAD and their artificial phantom analogues can be excited at 780 nm, and only FAD and its artificial phantom analogue can be excited at 880 nm. Also, the emission spectra of NADH and FAD are sufficiently similar to those of their chosen artificial phantom analogues.²¹

Literature on optical properties of human oral tissue in the relevant wavelength range proved to be sparse. Data was found for the human maxillary sinus as a graph³¹ and for different oral and colon tissues at 855 and 1064 nm. Values of μ'_s at the relevant wavelengths 780 and 880 nm were therefore derived from Bashkatov et al.³¹ with a digitizer tool³³ and used for calculating the composition of the scattering suspension.

To prepare scattering suspensions with optical parameters corresponding to human maxillary sinus according to Table 1 ($\mu'_{s,780\text{nm}} = 1.002 \text{ mm}^{-1}$ and $\mu'_{s,880\text{nm}} = 0.802 \text{ mm}^{-1}$), non-fluorescent spheres suspension and Pluronic solution were mixed in the ratios determined with the customized Matlab algorithm for Mie calculations based on literature^{27,28}, as described in section “Scattering medium”. To check the repeatability of the optical properties of the prepared scattering medium and their consistency with the respective target values, the scattering suspension for 780 nm was prepared three times and measured three times each, the suspension for 880 nm was prepared one time and measured three times using the existing integrating sphere setup²⁹ with modifications as described in section “Scattering medium”.

Imaging

The prepared structures were imaged using a multiphoton FLIM microscope (TCS SP8 DIVE FALCON multiphoton fluorescence lifetime microscope on an upright DM8 stand and a HC IRAPO L 25x/1.00 W motCORR objective, both Leica Microsystems GmbH), further referred to as multiphoton microscope MP-microscope. The microscope was equipped with a

TABLE 1 Literature values^{31,32} for human mucosa tissues; values for human maxillary sinus³¹ extracted using a digitizer tool³³

Tissue	λ (nm)	μ_a (cm ⁻¹)	μ_s (cm ⁻¹)	μ_s' (cm ⁻¹)	g
Oral mucosa: Normal Tissue ^{32,p283}	855	–	27 ± 11	2.7	0.9
Oral mucosa: Dysplastic Tissue ^{32,p283}	855	–	39 ± 6	3.9	0.9
Oral mucosa: Squamous cell carcinoma ^{32,p283}	855	–	60 ± 9	6	0.9
Colon: Muscle ^{32,p261}	1064	3.3	238	16.66	0.93
Colon: Submucous ^{32,p261}	1064	2.3	117	10.53	0.91
Colon: Mucous ^{32,p261}	1064	2.7	39	3.51	0.91
Colon: Integral ^{32,p261}	1064	0.4	261	15.66	0.94
Human maxillary sinus ³¹	780	0.17	–	10.02	0.9
Human maxillary sinus ³¹	880	0.14	–	8.02	0.9

motorized stage (Motorised Moveable Base Plate [MMBP], Scientifica Limited) and a titanium sapphire laser (Insight Dual 067, Spectra Physics). The fluorescent spheres were excited at 780 nm and their fluorescence was detected in the spectral regions 426–466 nm (further referred to as blue channel) and 542–582 nm (further referred to as green channel) by internal hybrid detectors (Leica HyD, pinhole open for multiphoton imaging). Additional imaging was done using the confocal part of the MP-microscope in reflection mode (imaging excitation laser at 500 nm, detection by internal photomultiplier, pinhole at 1 AU) to image the boundaries of the structure in x -direction for preliminary positioning and slope correction of the slide (the corresponding positions are indicated by two green squares in Figure 5).

To characterize the step structures, z -stacks were performed at selected x -positions between the two reference points, indicated exemplarily as small blue squares along the blue connecting line in Figure 5. At each selected position, a z -stack of either 20 or 40 μm height and 1 μm spacing along z was acquired with one of the settings listed in Table 2, resulting in identical lateral and axial resolution for every imaging stack. The image quality is not expected to change with increasing depth.³⁴ Nevertheless, an analysis was done to confirm that the designed artificial tissue phantom behaves according to expectations and no undesired effects are introduced. To check for a possible change in image quality with increasing imaging depth, from six different depths, five spheres per depths value and spectral detection channel were randomly chosen and their horizontal intensity profile extracted using LAS X (Leica Microsystems GmbH). These profiles were fitted with a Gaussian profile using Matlab. The mean and standard deviation (SD) of the obtained full width at half maximum (FWHM) were determined for each spectral detection channel. A Kruskal–Wallis test with $p > 0.05$ regarded as significant was done using Matlab to check whether the differences of the obtained FWHM values are significant.

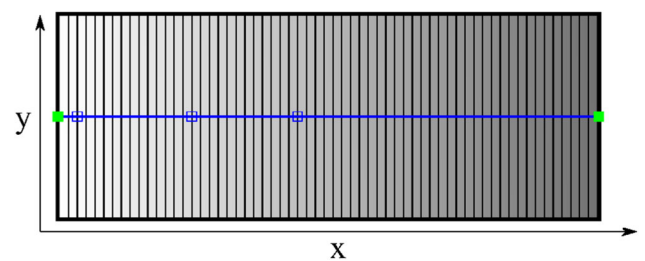


FIGURE 5 Scheme of imaging positions; green squares: imaging positions for slope correction; blue line: imaging direction along x -axes with exemplary indication of imaging stack positions.

Multiphoton images from within a scattering medium can generally be obtained from depths corresponding to two to three times the mean scattering free path l_s .^{3,34} For the chosen scattering parameter of $\mu_s'_{780\text{nm}} = 1.002 \text{ mm}^{-1}$ this would be up to $3 \times l_s \approx 300 \mu\text{m}$. It is therefore expected that multiphoton images can be acquired over the whole depth range of the step structures that exhibit a maximum depth of $65 \times 5 \mu\text{m} = 325 \mu\text{m}$.

A preliminary test with the FLIM part of the MP-microscope was conducted to check if sufficient numbers of photons for a successful fluorescence lifetime fit (fluorescence lifetime imaging of the fluorescent spheres results in clearly recognizable exponential decay curves and a successful fitting process) could be gathered within the entire depth range of the prepared structures. The fluorescence lifetime analysis and fitting was done using a mono-exponential decay function and binning 1 in the FLIM module of LAS X.

The MP-microscope system served as reference for the exemplary performance check. Images for assessing the aging of the prepared artificial phantom were acquired using the CF-microscope. Image preparation and analysis was done using Fiji,³⁵ LAS X, and Matlab.

To demonstrate the artificial tissue phantom is suitable for comparing different imaging systems,

Setting	Zoom factor	xy-pixel	FOV (μm)	xy resolution (μm)	z spacing (μm)
1	1	2048	442.86	0.21634	1.0
2	2	1024	221.43	0.21645	1.0

TABLE 2 List of used imaging parameters MP-microscope

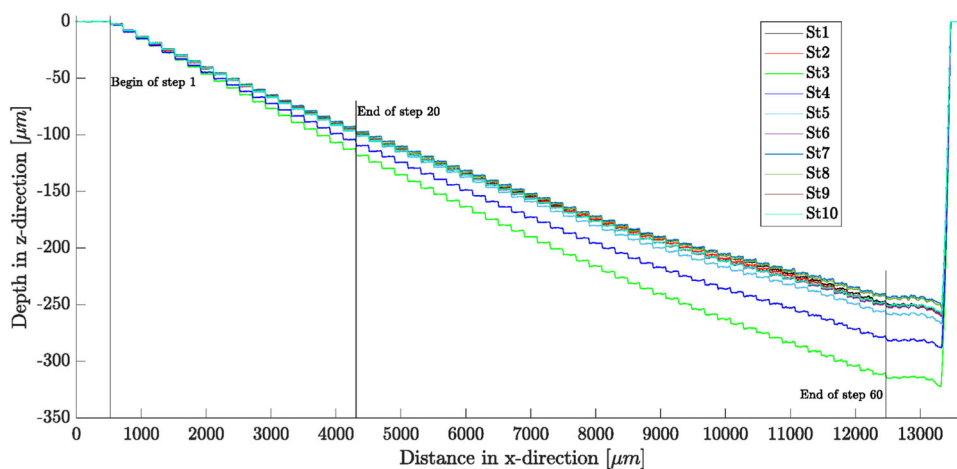


FIGURE 6 Depth profile of structured slides St1–St10.

including systems without z-stage, images were acquired using a modified FLIM platform for dermatology (MPTflex, JenLab GmbH). It contained two femto-second fiber lasers emitting at 780 and 880 nm (TOPTICA Photonics AG) and a hybrid detector (Becker&Hickl GmbH) and was equipped with a custom-made endoscope for the exploration of clinical applications, further referred to as FLIM-platform. In contrast to the microscopes, the FLIM-platform provided no tuneable spectral detection, but fluorescence signals were always collected within the broad wavelength range 409–660 nm by the FLIM detector. Thus, no further discrimination of fluorescence contributions was possible, apart from choosing one of two available excitation wavelengths. The recorded data were stored in Becker&Hickl *.sdt* files. To obtain time-integrated images, these files were imported into Fiji³⁵ and converted into an intensity image by integrating the photon numbers over all time channels for each pixel.

MP-microscope, CF-microscope, and FLIM-platform images of an artificial phantom were recorded to conduct a visual comparison of the resulting images.

RESULTS

Glass structure analysis

In Figure 6 the depth profile of the 10 analysed structured slides are shown. Between 61 and 63 steps per structure could be clearly distinguished by the implemented algorithm.

However, in the evaluation of the tread length and step height only the first 60 steps per structured slide were included, hence with the end of the 60th step there is no further descent but a hill-like structure with regular indentations, as can be seen in Figure 6.

With the exception of St3 and St4 the analysed structures overlap very well up to until step 20 ($x \approx 4000 \mu\text{m}$) and begin to deviate from there on. For St3 and St4 the edges of each step are still in the same positions in x-direction as for the other eight structures, but they start to deviate from those early, due to larger step heights.

The length of the treads of the individual structures are shown in Figure 7 as a function of the step index for the individual structures. They proved to be uniform with only slight deviations to the design of $200 \mu\text{m}$ length, the only exception being step number 41, which is $\approx 184 \mu\text{m}$ in length. Since this reduction in length occurs in all structures at the same position and to the same extent, it is likely to be caused by the manufacturing process, namely the programmed laser ablation pattern.

Mean values and standard deviations of the tread length L_i (59 per structure, as step 41 was excluded) are listed in Table 3.

The step heights are shown in Figure 8 as a function of the step number for the individual structures St1–St10. For all structures, the step height of the first step is ≈ 1 to $\approx 3 \mu\text{m}$, that of the second step is $\approx 6 \mu\text{m}$ and the step height decreases to $\approx 4 \mu\text{m}$ when reaching step 60. As seen in Figure 8, St3 and St4 deviate from the other structures by having a slightly higher step height in general, which explains the greater overall depth observed for these two

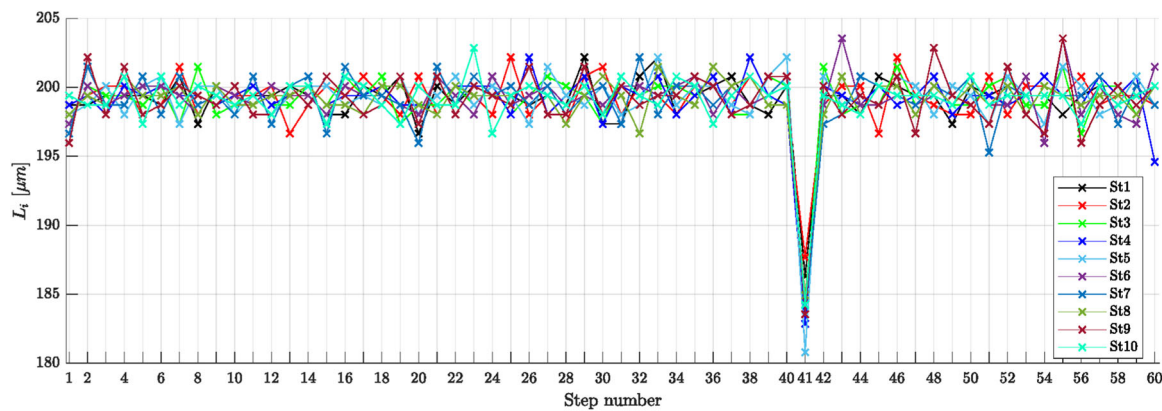


FIGURE 7 Tread length L_i of 60 steps from profiles St1–St10; the systematically shorter step 41 can clearly be distinguished.

TABLE 3 List of used imaging parameters MP-microscope

Structure	St1	St2	St3	St4	St5	St6	St7	St8	St9	St10	total
Mean (μm)	199.33	199.37	199.37	199.39	199.42	199.39	199.34	199.32	199.30	199.33	199.36
SD (μm)	1.1	1.22	1.18	1.17	1.21	1.27	1.44	1.00	1.59	1.11	1.23

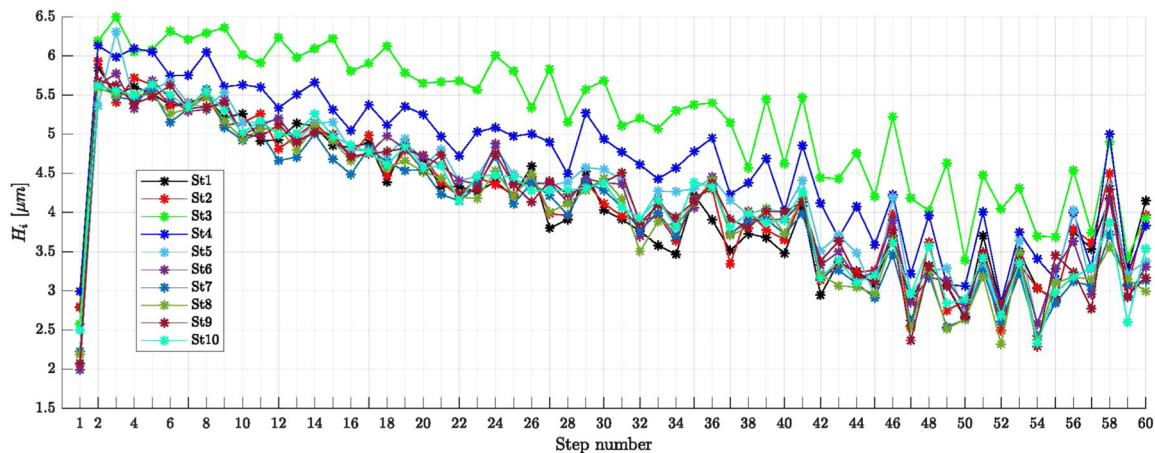


FIGURE 8 Step height H_i of individual steps for structures St1–St10; St3 and St4 deviate from the others due to overall higher step height.

structures in Figure 6. The steps of the other structured slides, except St3 and St4, follow each other with small variations.

Fluorescent spheres coating

The durability of the fluorescent spheres coating was checked during imaging with the MP-microscope in the imaged sample regions. One slide was kept in refrigeration after initial imaging with the multiphoton microscope, checking was done with the CF-microscope at random positions (excitation at 405 nm, detection ranges blue spheres 420–470 nm, yellow/green spheres 510–600 nm). Except for single fluorescent spheres, no

detachment of the coating could be detected in the examined areas, neither immediately after preparation or 14 days after preparation. Figure 9 shows a confocal image stack of the first two steps of structure St2 at 14 days after preparation. The steps are clearly distinguishable, and no detachment of the coating is visible.

Optical properties of scattering media

To prepare scattering suspensions with optical properties corresponding to human maxillary sinus according to calculations based on Table 1, 1 ml non-fluorescent spheres suspension was mixed with 5.33 ml water/Pluronic solution to obtain $\mu'_s = 1.002 \text{ mm}^{-1}$ at 780 nm

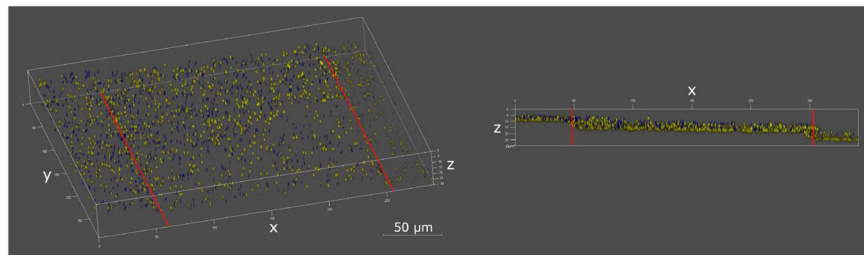


FIGURE 9 Structured slide St2, confocal image stack of fluorescent sphere coating 14 days after preparation (CF-microscope, $\lambda_{ex} = 405 \text{ nm}$, blue: blue fluorescent spheres, yellow: yellow/green fluorescent spheres), transitions between steps highlighted in red.

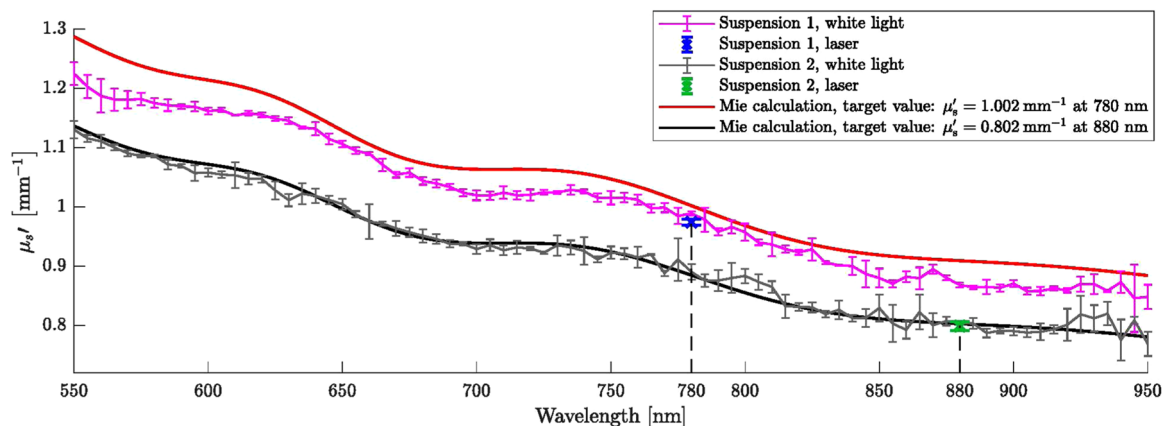


FIGURE 10 Mie calculation results for the reduced scattering coefficient of Suspensions 1 and 2 in comparison with integrating sphere measurements performed with a white light source and two laser diodes emitting light of 780 and 880 nm wavelength.

and with 6.17 ml water/Pluronic solution to obtain $\mu'_s = 0.802 \text{ mm}^{-1}$ at 880 nm, referred to as Suspension 1 and Suspension 2 in Figure 10. The optical properties of the resulting scattering suspensions were determined as described in section “Scattering medium” using an integrating sphere setup as described in section “Simulated optical properties”. In the case of the 780 nm suspension, only seven of the nine measurements conducted with the 780 nm laser diode were usable. A comparison of the measured μ'_s values and Mie calculations is shown in Figure 10 (mean and SD of three measurements per suspension). Overall, the measured values and corresponding Mie calculations are in reasonable agreement, although the deviations are clearly larger in the case of the suspension designed for 780 nm.

In Table 4 the μ'_s values for the two wavelengths are shown for different selections of the experimental results.

In Figure 11, transmission images of a phantom are shown that were obtained with the TLD of the CF-microscope within 2 hours after preparation and after 3 and 7 days of storage at room temperature, respectively. The images show that the non-fluorescent scattering spheres (black dots) tend to clot together over time and accumulate.

From the conducted experiments the timeframe for usability of the phantom is about one day from the time of applying the scattering medium. After this time period, the

TABLE 4 Mean values of μ'_s measured at 780 and 880 nm

Target Light source	$\mu'_s 780 \text{ nm} = 1.002 \text{ mm}^{-1}$		$\mu'_s 880 \text{ nm} = 0.802 \text{ mm}^{-1}$	
	$\mu'_s (\text{mm}^{-1})$ measured	n	$\mu'_s (\text{mm}^{-1})$ measured	n
WL	0.966 ± 0.021	9	0.8041 ± 0.0014	3
L	0.955 ± 0.020	7	0.7988 ± 0.0077	3
WL + L	0.961 ± 0.021	16	0.8015 ± 0.0057	6

Abbreviations: L, laserdiodes (780 and 880 nm, respectively); n , number of measurements; WL, white light source.

glass structure has to be cleaned and recoated, and new scattering medium has to be applied as described.

Imaging

A 3D rendering of a multiphoton imaging stack recorded with the MP-microscope around steps 9–10 (referring to a depth of 46 and 51 μm , respectively) within structured slide St5 is shown exemplarily in Figure 12. For the six steps listed in Table 5 together with the corresponding depths within the scattering medium, the brightest 2D image was extracted from the corresponding stack.

The first steps showed an increased density of fluorescent spheres compared to deeper ones. The laser power required to obtain an image from deeper areas was significantly increased.³⁶ However, a visual comparison

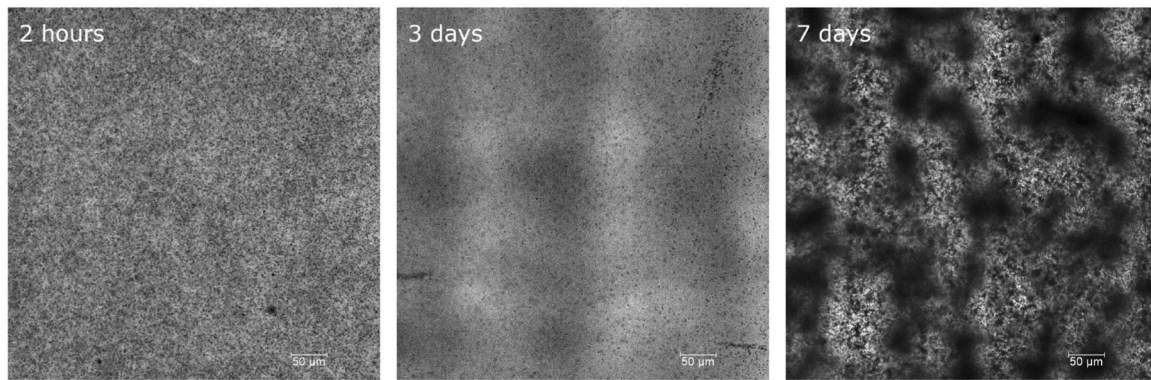


FIGURE 11 Detailed view of artificial phantom recorded at different times after preparation (2 hours, 3 days, and 7 days), at 2 hours the non-fluorescent spheres (black dots) are homogeneously distributed, at 3 days beginning of clotting is visible, at 7 days the non-fluorescent spheres are clotted to cloud like structures; CF-microscope, objective HC PL APO CS2 $\times 10/0.40$ DRY, FOV 516.67 μm ; x/y resolution 0.5 $\mu\text{m}/\text{pixel}$; scale bar is 50 μm .

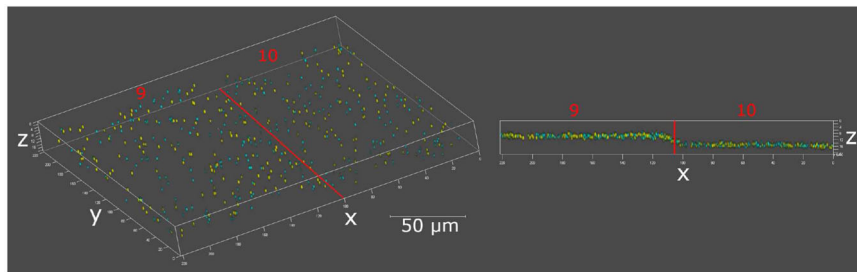


FIGURE 12 Structured slide St5 with scattering medium, steps 9 and 10 referring to depth of 46 and 51 μm , respectively; steps 9 and 10 marked and transition between steps highlighted by a red line in left image; MP-microscope, $\lambda_{ex} = 780$ nm, cyan: blue fluorescent beads, yellow: yellow/green fluorescent beads.

TABLE 5 Mean and standard deviation of FWHM of five fluorescent spheres per depth and channel and relative laser-power for excitation at 780 nm for images of six steps at increasing depth (MP-microscope).

Step	1	10	19	29	39	59
Depth (μm)	2	52	96	142	184	252
FWHM blue channel (mean \pm SD) μm	0.773 \pm 0.097	0.79 \pm 0.11	0.83 \pm 0.16	0.83 \pm 0.11	0.88 \pm 0.10	0.77 \pm 0.14
FWHM green channel (mean \pm SD) μm	0.817 \pm 0.020	0.771 \pm 0.019	0.785 \pm 0.031	0.753 \pm 0.044	0.789 \pm 0.023	0.788 \pm 0.076
Relative laser power (% AOM)	0.5	0.8	1.7	3.6	5.4	21

shows, as expected from literature,³⁴ no detectable degradation of image quality with increasing depth. To confirm this, from each depth listed in Table 5, five spheres per depth value and spectral detection channel as described in chapter "Imaging" were randomly chosen and their horizontal intensity profile extracted and fitted with a Gaussian profile to retrieve the FWHM. The mean and SD of the obtained FWHM values for each spectral detection channel are collected in Table 5. The performed Kruskal–Wallis test on the FWHM values obtained for every depth and channel (blue channel: $p = 0.7684$, green channel: $p = 0.1269$) showed no difference between the six imaging depths, which confirms the visual impression of basically constant image quality

regardless of depth and is therefore consistent with the expected behaviour.⁴ The SD is found to be systematically larger for the blue channel. This is probably caused by the blue fluorescent beads being less excitable at the chosen wavelength, which was deliberately desired as described in the chapter "Fluorescent sphere coating".

A preliminary FLIM test with the MP-microscope, excitation wavelength of 780 nm, was carried out on one structured slide with scattering medium. It was possible to obtain FLIM images from the whole depth range of the structure and to obtain a useful fluorescence lifetime fit in both the blue and the green detection channel. Fluorescence lifetime fitting was done monoexponentially with binning 1.

The depth positions and obtained fluorescence lifetime values of the fluorescent beads are shown in Table 6 and graphically in Figure 13. The fluorescence lifetimes are different for the two kinds of fluorescent spheres, which is not unexpected since they contain different fluorophores. The measured fluorescence lifetimes are shorter between 2.1 and 23.2 μm depth compared to the lifetime values obtained from depth 0 μm (without scatterer overlaying the fluorescent spheres) for both spectral detection channels. The measured fluorescence lifetimes increase at a depth of 49.8 μm and decrease from there on until the deepest measured point (238.8 μm). For both spectral detection channels, the observed change of fluorescent lifetime with depth is greater than the SD of the data. Additionally, the change in fluorescence lifetime is almost equal for both channels in a way that the difference between the two fluorescent lifetimes does not change with increasing depth but stays relatively constant at (0.800 ± 0.048) ns.

Due to the different nature of the imaging systems included in the comparison between the MP-microscope, CF-microscope and the FLIM-platform, it was not possible to capture images of the glass structures with the same imaging parameters, specifically magnification, number of pixels and detection filters, as mentioned in the description of the FLIM-platform.

The exemplary comparison of three pairs of images representing two depths (Z1 and Z2) within an artificial phantom with scattering medium coated with fluorescent spheres (1 μm diameter) recorded with three imaging devices (MP-microscope, CF-microscope, FLIM-platform)

is shown in Figure 14. These are the time-integrated images recorded with the FLIM-platform, confocal images recorded with the same spatial resolution (CF-microscope, excitation 405 nm, detection range 510–600 nm) as the FLIM-platform and images recorded with the MP-microscope (with the spatial resolution according to setting 2 in Table 2). A precise comparison of the imaging quality between the FLIM-platform (and also the CF-microscope) and the MP-microscope is not possible based on these images, because the scan point densities were different and in case of the FLIM-platform (and also the CF-microscope) not high enough to fulfil the sampling theorem³⁷ with respect to the available optical resolution and the size of the fluorescent spheres. The on-purpose equally undersampled images obtained with the CF-microscope (see Figure 14) show similar structures as those recorded with the FLIM-platform, so at least a comparison at this level is possible. This comparison reveals a few differences. In the FLIM-platform image recorded at Z1 position, it looks like the focal plane is cylinder-shaped with the cylinder axis pointing along y , whereas the image recorded at Z2 position seems to have a slight slope along the y -direction, and from the middle of the image upward, similarly represented fluorescent spheres seem to be arranged along a roughly semicircular bent grid. In the images recorded with the CF-microscope the two z -positions are clearly distinguishable by the fact that fluorescent spheres, resting on two adjacent treads, are in the focus and thus visible only on the left (Z1 position) or on the right (Z2 position) of the step edge, respectively, highlighted by a red line at the transition between the steps in the figure.

Fluorescence lifetime (ns)					
Depth (μm)	0	2.1	23.2	49.8	97.8
Blue channel	2.736 \pm 0.062	2.639 \pm 0.038	2.627 \pm 0.045	2.759 \pm 0.032	2.659 \pm 0.037
Green channel	3.584 \pm 0.102	3.417 \pm 0.055	3.422 \pm 0.033	3.588 \pm 0.039	3.444 \pm 0.048
Depth (μm)	140.3	178.7	210.2	238.8	
Blue channel	2.545 \pm 0.024	2.407 \pm 0.035	2.411 \pm 0.031	2.322 \pm 0.040	
Green channel	3.385 \pm 0.032	3.265 \pm 0.041	3.168 \pm 0.047	3.034 \pm 0.049	

TABLE 6 of the fluorescent beads in the blue and the green detection channel in scattering medium with measured $\mu'_s 780\text{nm} = 0.96 \text{ mm}^{-1}$, MP-microscope, excitation wavelength 780 nm.

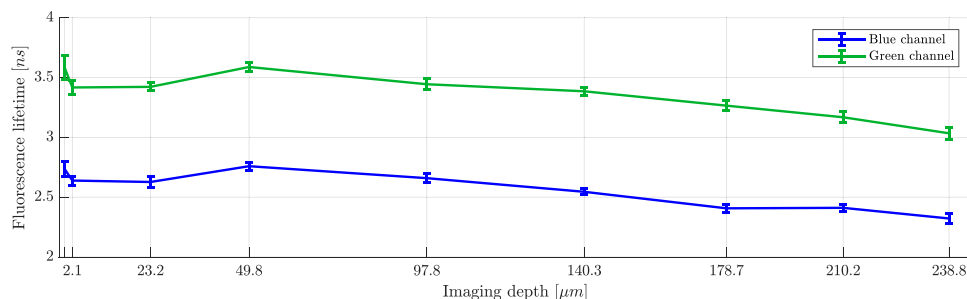


FIGURE 13 Fluorescence lifetime obtained from blue and green detection channels versus depths; individual values see Table 6; fluorescent lifetimes of the blue and green channel over increasing imaging depths.

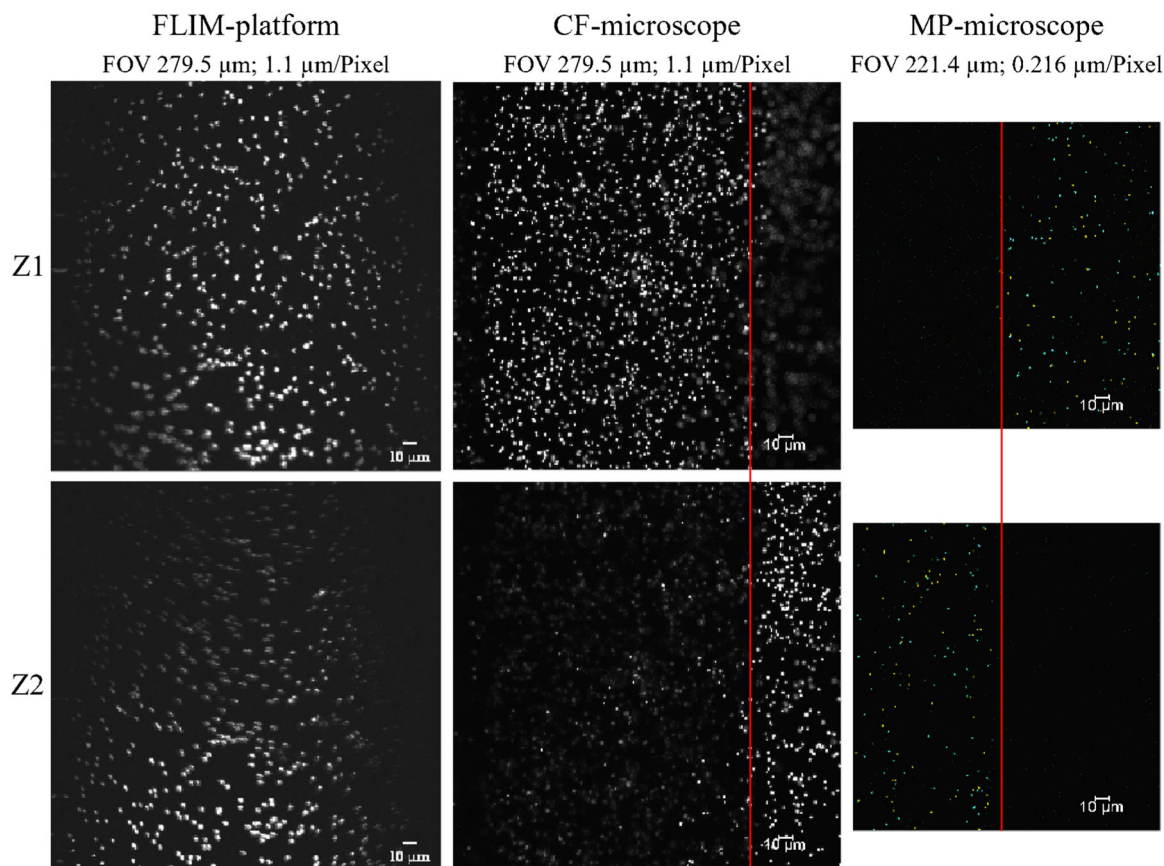


FIGURE 14 Comparison of images obtained with the FLIM-platform (left) and the CF-microscope (middle) with the same field of view (FOV) and resolution settings and the MP-microscope (imaging parameters see Table 2 setting 2) at two different z -positions; images are sized to have the same scale; histogram stretching was applied to increase the contrast of the images (original data are provided in the Supporting Information Material); visible transitions between steps in the images are highlighted by red line; CF-microscope objective HC PL APO CS2 40x/1.30 OIL.

In the case of the MP-microscope with $NA = 1.0$ used for generating the images excited at 780 nm and shown in Figure 14 (3rd column), the theoretical³⁸ lateral and axial resolution are ≈ 330 nm and ≈ 1400 nm, respectively, which provides the demanded resolution for resolving spheres of 1 μ m diameter (corresponding to the size of mitochondria in cells). The images were recorded with a lateral scanning resolution of 0.216 μ m and are consistent with the specified theoretical resolution. In case of the CF-microscope with $NA = 1.3$ used for generating the images in Figure 14 (2nd column), the theoretical³⁹ lateral and axial resolution are ≈ 160 nm and ≈ 480 nm, respectively, which also meets the specifications for resolving spheres of 1 μ m diameter. However, for direct comparability of the images, the lateral scan resolution was set to 1.1 μ m/pixel to match the scan resolution with that of the FLIM-platform. In contrast to the MP- and CF-microscope, the NA of the custom-built FLIM-platform was not known, but assumed to be >0.5 , so that at least a lateral and axial resolution of ≈ 670 nm and ≈ 5800 nm could be expected. Such lateral resolution would be sufficient for resolving mitochondria of about 1 μ m diameter as desired, but could not be taken as

granted. Since the scan-resolution of the FLIM-platform was fixed at 1.1 μ m/pixel, the lateral resolution could not be determined quantitatively.

DISCUSSION

It was the objective of the current study to create an artificial phantom which enables the comparison of different imaging systems in a reproducible way. The primary intention of the development was to quantify the maximum imaging depth reachable with a given optical system. The maximum imaging depth is limited, on one hand, by the mechanical contact between sample and objective, on the other hand, via the demand of a certain signal-to-noise level, by the available laser power and integration time. Which of these two limitations is reached first for a given system/sample combination depends on the optical system (supplied light intensity, focus quality, light collection, and detection efficiency) and on the optical properties of the sample, in this study of the scattering layer (adaptable to mimic different types of tissue) above the fluorescent beads. A determination

of the optical resolution was originally not intended since it was not expected to change with imaging depth.³⁴ But it would be of interest to deepen the investigation in this regard taking the intensity distribution of the fluorescent beads in scattering media into account, which is described in Durr et al.³⁴ and Dunn et al.⁴⁰

To reach the specified objective, fluorescent beads were arranged within surface-parallel treads at different, but well-known depths within a medium. The bead positions within these sheets are arbitrary, but time-independent, because the beads are fixed on the surface of the prepared treads. The geometry of the treads is determined by the morphology of the laser-manufactured structures. The characterization of the glass structures indicates a good reproducibility of the manufacturing process with regard to the tread length of the inscribed steps, whereas the step height varies considerably and systematically with the step-index. By suitable characterization, however, the depth of each individual tread below the surface of the glass substrate can be determined, so the variation of the step height does not reduce the functionality of the artificial phantom. For enhanced ease of use, a refinement of the manufacturing protocol would be desirable to achieve a constant step height for all steps. The variability of the tread length is very small, as seen in Table 3 ($[199.36 \pm 1.23] \mu\text{m}$ for all 590 individual steps). This very small variability should not affect the usability of the phantoms for the intended purpose of depth-dependent optical characterizations. In addition, the treads are slightly inclined with respect to the surface of the glass substrate, which could also be characterized with additional effort, if needed. Furthermore, the treads are not perfectly smooth, but slightly rough on a $\approx 1 \mu\text{m}$ micrometer scale, as expected for the used laser microstructuring technique.⁴¹ In comparison to the step height of about $5 \mu\text{m}$, this roughness did not affect the functionality of the artificial phantom in this study. The same holds for the step flatness, which, according to Figure 6, obviously increases with increasing depth, but remains smaller than the step height for all depths up to step 60. This is obviously not crucial, given that the axial resolution in the case of the experiments with the FLIM-platform was theoretically estimated to be $\approx 5800 \text{ nm}$. However, the step flatness may pose a limitation in the characterization of imaging systems, depending on the axial resolution of the system under investigation. Due to the mentioned limitations, it might be worthwhile to also explore alternative manufacturing processes like etching⁴² or multiphoton lithography.⁴³

The method chosen to fix the fluorescent beads on the prepared treads follows a known approach in the field of microscopy for the fixation of micro- or nanoparticles to surfaces.⁴⁴ The fixation of the fluorescent beads proved to be stable for at least 14 days and the PVA did obviously not inhibit their fluorescence. The fluorescent beads were chosen based on the similarity of their spectral excitation and emission characteristics with

those of NADH and FAD, because the phantom was codeveloped with the modification of a multiphoton tomography system for metabolic FLIM investigations.^{45,46} The prepared structures are not limited to this use case, since fluorescent spheres are available in a variety of diameters and spectral excitation and emission characteristics. These properties can be chosen to match the requirements for the system to be tested. The proposed phantom was especially designed for mimicking features encountered when trying to optically diagnose the metabolic states of cells within the epithelial layers in the upper respiratory tract. A minimum accessible depth range of $\approx 100 \mu\text{m}$ was desired in the present case. The optical properties of biological tissue reported in literature vary considerably, even for one specific species, tissue type and tissue state.³² For the primary target tissues of this study, the mucosa of human larynx and especially human vocal cords, optical parameters were not available from literature for the used wavelengths which were adapted to the excitation wavelength used for the target chromophores (NADH and FAD) in metabolic imaging. Instead, literature values for human maxillary sinus³² were chosen, as those were available for the used wavelengths. The reduced scattering coefficients μ'_s of the different tissues may differ slightly, but were deemed to be similar enough for this study, especially when keeping in mind that the crucial characteristic of a phantom is the reproducibility of its properties, rather than exactly matching property values.¹

To mimic the scattering behaviour of biological tissue, embedding polymer microspheres in a medium of different refractive index is widely used,¹ because it is conceptually simple and the scattering behaviour can be calculated analytically using Mie theory and thereby conveniently adjusted via suitable selection of compositions and particle diameters.^{26,27} In Figure 10, the measured data curve for the scattering suspension designed for excitation at 880 nm follows the Mie calculation with only slight deviations. The measured values for the suspension designed for excitation at 780 nm are lower than those of the Mie calculation, and in the range 550–750 nm, the measured curve appears slightly shifted and/or squeezed along the wavelength axis with respect to the curve obtained from Mie calculation. The cause for this observation could not be ascertained as both suspensions were mixed from the same stock materials, and the same Mie calculation algorithm was used for both compositions. Despite the observed deviation, the difference between measurement and calculation is within acceptable limits considering that the refractive indices of the Pluronic solution and the non-fluorescent beads could differ from the assumptions made for the calculations. The integrating sphere measurement system²⁹ used for determining the optical parameters of the scattering medium is based on the adding-doubling method that is known to yield optical parameters with a

precision of 2%–3%.⁴⁷ With this in mind, the reproducibility of the reduced scattering coefficient of the scattering medium is as expected ($\mu'_s = (0.96 \pm 0.02) \text{ mm}^{-1}$ for 780 nm and $\mu'_s = (0.8 \pm \epsilon) \text{ mm}^{-1}$ with $\epsilon < 0.008$) mm^{-1} for 880 nm, see Table 4). Furthermore, the deviation of these measured values of μ'_s and the respective target values (1.002 and 0.802 mm^{-1} , respectively, see also Table 4) is acceptable.

The concentration of the Pluronic solution in which the polymer microspheres were dissolved to form the scattering medium was a compromise between the mechanical and temporal stability of the phantom and the feasibility of preparation and handling of the medium. The ability of Pluronic to form a gel and the stiffness of the resulting gel depends on concentration and temperature.^{48–50} Exploratory attempts to immobilize fluorescent beads within a microchannel (μ -Slide VI 0.4, Cat. no. 80606, ibidi GmbH) were performed with a 20%w/w Pluronic/water solution, which forms a relatively stiff gel. These experiments showed no detectable sedimentation of the fluorescent beads for approximately 10 months if kept at room temperature. Preparing the scattering medium with Pluronic solutions of such high concentrations, however, proved to be very time-consuming (approx. 1 week for preparing one scattering dispersion) and made it very difficult to apply the medium to the glass structures, because this required cooling the syringes or pipettes and/or the glass structure to $\approx 1^\circ\text{C}$ to assure a homogeneous distribution of the medium within the glass structure. Suspensions of non-fluorescent beads in pure water, however, sedimented within an hour after preparation and applying the cover glass. Therefore, as a compromise, a 13%w/w Pluronic solution was finally used to prepare the phantoms. At this concentration the solution forms a viscous fluid at room temperature that is relatively easy to apply and kept the non-fluorescent beads in suspension long enough to conduct all necessary imaging experiments. The resulting durability of the phantom of about 1 day is nevertheless not satisfactory. Therefore in a further development of the scattering medium formulation it should be tried to increase the Pluronic concentration to a point where the solutions are still relatively easy to prepare and handle, but result in a longer suspension time of the non-fluorescent beads. Alternatively, another matrix material for the scattering layer, like silicon resins or a different hydrogel may be investigated in terms of usability and durability.

Multiphoton images could be obtained from depth up to $\approx 300 \mu\text{m}$, corresponding to $3 \times l_s$, within the scattering medium, which is consistent with literature. The image quality was found, as expected in accordance with literature, to not decrease with increasing depth. Both findings prove that the designed artificial tissue phantom behaves as expected from theory based on its design parameters and literature. The observed change in

fluorescence lifetime with increasing depth for both types of fluorescent beads adhered to the steps of the structured glass slides is unlikely to be caused by a quenching effect, because the environment surrounding the spheres does not change chemically with increasing depth. They are only buried deeper inside the scattering medium. The equal change in fluorescent lifetime versus depths for both fluorescent beads indicates that the cause of the lifetime change is present at and equal for both types of beads and both detectors used, since they are affected in the same way. The only apparent difference, set aside the necessary increase in excitation laser power to be able to excite the fluorescent beads, is the increasing amount of scattering medium on top of the fluorescent beads and therefore a change in system geometry. Since a change of geometry can influence fluorescent lifetimes measured in scattering media,⁵¹ it is assumed that this is the cause for the observed changes in fluorescent lifetime. To study these effects further was not the scope of the presented work. These findings have to be addressed in further studies since techniques like metabolic imaging depend on the accurate determination of fluorescence lifetimes and are, if used in vivo, likewise conducted in scattering tissue. Therefore, geometry-related shifts in the apparent/fitted fluorescent lifetimes of the involved fluorophores should be taken into consideration in such investigations.

The performed feasibility test of comparing MP-, CF-microscope and FLIM-platform incl. endoscope should show how a potential characterization scenario could look like for a system with unknown properties and if any differences between a known and an unknown system become recognizable as shown in Figure 14. It was possible to obtain images of the prepared step structures with the FLIM-platform and the custom-made endoscope. A direct comparison of the spatial resolution between the MP-microscope and the FLIM-platform was unfortunately not possible due to limitations in the instrument settings of the FLIM-platform. Therefore, additional images were recorded with the CF-microscope, with a spatial resolution corresponding to that of the FLIM-platform. The comparison revealed a reduced image quality of the FLIM-platform. It was not possible to distinguish adjacent steps with this system, the images seemed to be vignetted, a kind of a cylindrical distortion was observed in the images, and the fluorescent beads exhibited semicircular shapes in some areas of the images. Images recorded with this system on real biological tissue showed similar artifacts. Simulation data and transmitted light images of an USAF target made with the custom-made endoscope showed no severe distortions.

Also, an examination of immobilized fluorescent beads at a multiphoton microscope (system described previously²¹) did not indicate that using a cling film instead of a cover glass would distort the images in a way as seen with the FLIM-platform. Therefore, it is assumed that optical components upstream from the endoscope or a mismatch

of the interface between endoscope and FLIM-platform are responsible for the observed features and distortions. This should be part of further investigations.

The developed concept of a modifiable artificial tissue phantom based on a microstructured slide proved to be promising to be able to compare different microscopic and microendoscopic imaging devices and should be explored and developed in further studies.

The maximum imaging depth of a particular system/sample combination can be determined by recording images of the steps inside the phantom, starting from the level of the cover slip and descending the staircase structure step by step, until the image quality drops below an acceptable level (or a mechanical contact between objective and sample occurs). This procedure is also conceivable with endoscope and microendoscope systems. By matching the optical properties of the proposed phantom to the properties of the tissue of interest and the fluorescent beads to the excitation wavelengths of interest, it should be possible to characterize, for example, the depth of field and the maximally reachable imaging depth of endoscopes and micro-endoscopes for fluorescence-assisted diagnosis and treatment.^{52–54}

Potential other areas of application could be the characterization of hyperspectral imaging (HSI) cameras, especially endoscopic versions thereof. By replacing the fluorescent by an absorptive coating and adapting the geometric dimensions of the structure, it is conceivable to examine which perfusion parameter⁵⁵ determined by the HSI camera can be measured up to which depth in the tissue phantom and, thus, also in vivo. The possible applications are not limited to the ones stated above and should be explored further.

CONCLUSION

In general, laser-machined glass structures could be successfully used to characterize differences in the imaging quality of an endoscopic two-photon FLIM system under development and a high-end research microscope as a reference, as well as to identify possible problems and the related system components. The challenge in designing artificial tissue phantoms for high spatial resolution imaging systems is the adaptation to the specific intended use. Based on the investigation reported here, a large range of different systems could be experimentally characterized with the proposed phantom.

ACKNOWLEDGMENTS

The authors thank J. Janusch, T. Kellerer, M. Saller, S. Dietzel and M. G. Pisfil for their assistance, the Core Facility Bioimaging at the Biomedical Center (BMC) of the Ludwig-Maximilians Universität München (LMU), microscope system funded by a grant of the Deutsche

Forschungsgemeinschaft (DFG) (INST 86/1909-1) as well as the Core Facilities of the Musculoskeletal University Center Munich of the Ludwig-Maximilians-Universität München (LMU), microscope system funded by a grant of the Deutsche Forschungsgemeinschaft (DFG) (409-220-1 FUGG) and D. Smeets (Leica Microsystems) for discussions and advice. The work described in this manuscript was performed with the support of the German Federal Ministry of Education and Research (BMBF, project OMOXI, grant no. 13N14507). S. Ströbl was financially supported by Österreichische Forschungsförderungsgesellschaft (grant no. 855657). M. Aumiller was financially supported by the German Research Foundation (DFG) within research training group (RTG) GRK2274. Open Access funding enabled and organized by Projekt DEAL.

CONFLICT OF INTEREST

The authors declare no conflict of interest.

ORCID

Christian Freymüller  <https://orcid.org/0000-0002-3014-297X>

Stephan Ströbl  <https://orcid.org/0000-0002-0384-0318>

Maximilian Aumiller  <https://orcid.org/0000-0002-1343-6669>

Maximilian Eisel  <https://orcid.org/0000-0002-7321-7302>

Ronald Sroka  <https://orcid.org/0000-0001-7952-2407>

REFERENCES

1. Pogue BW, Patterson MS. Review of tissue simulating phantoms for optical spectroscopy, imaging and dosimetry. *J Biomed Opt.* 2006;11:041102.
2. Markwardt NA, Haj-Hosseini N, Hollnburger B, Stepp H, Zelenkov P, Rühm A. 405 nm versus 633 nm for protoporphyrin IX excitation in fluorescence-guided stereotactic biopsy of brain tumors. *J Biophoton.* 2016;9:901–912.
3. Theer P, Denk W. On the fundamental imaging-depth limit in two-photon microscopy. *J Optical Soc Am A.* 2006;23:3139.
4. Dong C-Y, Koenig K, So P. Characterizing point spread functions of two-photon fluorescence microscopy in turbid medium. *J Biomed Opt.* 2003;8:450.
5. Fixler D, Nayhoz T, Ray K. Diffusion reflection and fluorescence lifetime imaging microscopy study of fluorophore-conjugated gold nanoparticles or nanorods in solid phantoms. *ACS Photon.* 2014;1:900–905.
6. Wang D, Chen Y, Liu JTC. A liquid optical phantom with tissue-like heterogeneities for confocal microscopy. *Biomed Opt Express.* 2012;3:3153.
7. König K, Ehlers A, Riemann I, Schenkl S, Bückle R, Kaatz M. Clinical two-photon microendoscopy. *Microsc Res Techniq.* 2007;70:398–402.
8. Bao H, Allen J, Pattie R, Vance R, Gu M. Fast handheld two-photon fluorescence microendoscope with a 475 $\mu\text{m} \times 475 \mu\text{m}$ field of view for in vivo imaging. *Opt Lett.* 2008;33:1333–1335.
9. Kiekens KC, Romano G, Galvez D, et al. Reengineering a falloposcope imaging system for clinical use. *Transl Biophoton.* 2020;2: e202000011.
10. Weyers BW, Marsden M, Sun T, et al. Fluorescence lifetime imaging for intraoperative cancer delineation in transoral robotic surgery. *Transl Biophoton.* 2019;1:e201900017.

11. Huizen LMG, Radonic T, Mourik F, et al. Compact portable multiphoton microscopy reveals histopathological hallmarks of unprocessed lung tumor tissue in real time. *Transl Biophoton.* 2020;2: e202000009.
12. Anastasopoulou M, Koch M, Gorpas D, et al. Comprehensive phantom for interventional fluorescence molecular imaging. *J Biomed Opt.* 2016;21:091309.
13. Gorpas D, Koch M, Anastasopoulou M, Klemm U, Ntziachristos V. Benchmarking of fluorescence cameras through the use of a composite phantom. *J Biomed Opt.* 2017;22:016009.
14. Hinsdale T, Olsovsky C, Rico-Jimenez JJ, Maitland KC, Jo JA, Malik BH. Optically sectioned wide-field fluorescence lifetime imaging microscopy enabled by structured illumination. *Biomed Opt Express.* 2017;8:1455.
15. Markwardt NA, Stepp H, Franz G, et al. Remission spectrometry for blood vessel detection during stereotactic biopsy of brain tumors. *J Biophoton.* 2017;10:1080–1094.
16. Chen AI, Balter ML, Chen MI, et al. Multilayered tissue mimicking skin and vessel phantoms with tunable mechanical, optical, and acoustic properties. *Med Phys.* 2016; 43:3117–3131.
17. Pinkert MA, Cox BL, Dai B, Hall TJ, Eliceiri KW. 3-D-printed registration phantom for combined ultrasound and optical imaging of biological tissues. *Ultrasound Med Biol.* 2020;46: 1808–1814.
18. Horng H, O'Brien K, Lamont A, Sochol RD, Pfefer TJ, Chen Y. 3D printed vascular phantoms for high-resolution biophotonic image quality assessment via direct laser writing. *Opt Lett.* 2021;46:1987.
19. Nečas D, Klapetek P. Gwyddion: an open-source software for SPM data analysis. *Open Phys.* 2012;10.
20. Gwyddion—Free SPM (AFM, SNOM/NSOM, STM, MFM, ...) data analysis software. Available from: <http://gwyddion.net/download.php#stable-windows>. Accessed 12 Aug 2020.
21. Freymüller C, Kalinina S, Rück A, Sroka R, Rühm A. Quenched coumarin derivatives as fluorescence lifetime phantoms for NADH and FAD. *J Biophoton.* 2021;14:e202100024.
22. Daimon M, Masumura A. Measurement of the refractive index of distilled water from the near-infrared region to the ultraviolet region. *Appl Opt.* 2007;46:3811.
23. Refractive index of H₂O, D₂O (Water, heavy water, ice)—Daimon-20.0C. Available from: <https://refractiveindex.info/?shelf=main&book=H2O&page=Daimon-20.0C>. Accessed 5 Nov 2020.
24. Sultanova NG, Kasarova SN, Nikolov ID. Characterization of optical properties of optical polymers. *Optical Quantum Electron.* 2013;45:221–232.
25. Refractive index of (C₈H₈)_n (Polystyrene, PS)—Sultanova. Available from <https://refractiveindex.info/?shelf=organic&book=polystyren&page=Sultanova>. Accessed 8 Aug 2020.
26. Mie G. Beiträge zur Optik trüber Medien, speziell kolloidaler Metallösungen. *Annalen der Physik.* 1908;330:377–445.
27. Maetzel's MATLAB code for Mie theory. Available from <https://omlc.org/software/mie/>. Accessed 23 Aug 2019.
28. Bohren CF, Huffman DR. Absorption and scattering of light by small particles. 1st ed. Wiley; 1998.
29. Eisel M, Ströbl S, Pongratz T, Stepp H, Rühm A, Sroka R. Investigation of optical properties of dissected and homogenized biological tissue. *J Biomed Opt.* 2018;23:1.
30. Lemaillet P, Bouchard J-P, Hwang J, Allen DW. Double-integrating-sphere system at the national institute of standards and technology in support of measurement standards for the determination of optical properties of tissue-mimicking phantoms. *J Biomed Opt.* 2015;20:121310.
31. Bashkatov AN, Genina ÉA, Kochubey VI, et al. Optical properties of mucous membrane in the spectral range 350–2000 nm. *Opt Spectrosc.* 2004;97:978–983.
32. Tuchin VV. Tissue optics: light scattering methods and instruments for medical diagnosis. Bellingham, WA: SPIE; 2015.
33. Rohatgi A. Webplotdigitizer: Version 4.3; 2020. Available from: <https://automeris.io/WebPlotDigitizer/index.htm>.
34. Durr NJ, Weisspennig CT, Holfeld BA, Ben-Yakar A. Maximum imaging depth of two-photon autofluorescence microscopy in epithelial tissues. *J Biomed Opt.* 2011;16:026008.
35. Schindelin J, Arganda-Carreras I, Frise E, et al. Fiji: an open-source platform for biological-image analysis. *Nat Methods.* 2012;9:676–682.
36. Berrocal E, Sedarsky DL, Paciaroni ME, Meglinski IV, Linne MA. Laser light scattering in turbid media part I: experimental and simulated results for the spatial intensity distribution. *Opt Express.* 2007;15:10649.
37. Benedetto JJ, Ferreira PJSG, editors. Modern sampling theory. Boston: Birkhäuser; 2001.
38. Young MD, Field JJ, Sheetz KE, Bartels RA, Squier J. A pragmatic guide to multiphoton microscope design. *Adv Opt Photon.* 2015;7:276.
39. Amos B, McConnell G, Wilson T. 2.2 confocal microscopy. In: Comprehensive biophysics, Elsevier; 2012. p. 3–23.
40. Dunn AK, Wallace VP, Coleno M, Berns MW, Tromberg BJ. Influence of optical properties on two-photon fluorescence imaging in turbid samples. *Appl Opt.* 2000;39:1194.
41. Wang T, Chen J, Zhou T, Song L. Fabricating microstructures on glass for microfluidic chips by glass molding process. *Micromachines.* 2018;9:269.
42. Hülsenberg D, Harnisch A, Bismarck A. Microstructuring of glasses; Vol 87 of *Springer Series in Materials Science*. Berlin, Heidelberg: Springer; 2008.
43. Harinarayana V, Shin YC. Two-photon lithography for three-dimensional fabrication in micro/nanoscale regime: a comprehensive review. *Opt Laser Technol.* 2021;142:107180.
44. Talbot CB, Patalay R, Munro I, et al. Application of ultrafast gold luminescence to measuring the instrument response function for multispectral multiphoton fluorescence lifetime imaging. *Opt Express.* 2011;19:13848.
45. Kalinina S, Bisinger D, Breyer J, Rück A. Cell metabolism, FLIM and PLIM and applications. In: Periasamy A, So PTC, König K, editors. Multiphoton microscopy in the biomedical sciences XV. Vol. 9329. San Francisco, CA: International Society for Optics and Photonics SPIE; 2015. p. 39–43.
46. Kalinina S, Freymüller C, Naskar N, et al. Bioenergetic alterations of metabolic redox coenzymes as NADH, FAD and FMN by means of fluorescence lifetime imaging techniques. *Int J Mol Sci.* 2021;22:5952.
47. Prahl SA, Gemert MJC, Welch AJ. Determining the optical properties of turbid media by using the adding-doubling method. *Appl Opt.* 1993;32:559.
48. Gioffredi E, Boffito M, Calzone S, et al. Pluronic F127 hydrogel characterization and biofabrication in cellularized constructs for tissue engineering applications. *Proc CIRP.* 2016;49:125–132.
49. Suntornnond R, Tan EYS, An J, Chua CK. A highly printable and biocompatible hydrogel composite for direct printing of soft and perfusable vasculature-like structures. *Sci Reports.* 2017;7: 16902.
50. Schmolka IR. Artificial skin I. Preparation and properties of pluronic F-127 gels for treatment of burns. *J Biomed Mater Res.* 1972;6:571–582.
51. Nishimura G, Awasthi K, Furukawa D. Fluorescence lifetime measurements in heterogeneous scattering medium. *J Biomed Opt.* 2016;21:075013.
52. Waidelich R, Stepp H, Baumgartner R, Weninger E, Hofstetter A, Kriegmair M. Clinical experience with 5-aminolevulinic acid and photodynamic therapy for refractory superficial bladder cancer. *J Urol.* 2001;165:1904–1907.

53. Stummer W, Stepp H, Möller G, Ehrhardt A, Leonhard M, Reulen HJ. Technical principles for protoporphyrin-IX-fluorescence guided microsurgical resection of malignant Glioma tissue. *Acta Neurochirurgica*.1998;140:995–1000.
54. Stepp H, Stummer W. 5-ALA in the management of malignant glioma. *Lasers Surgery Med*. 2018;50:399–419.
55. Kulcke A, Holmer A, Wahl P, Siemers F, Wild T, Daeschlein G. A compact hyperspectral camera for measurement of perfusion parameters in medicine. *Biomed Eng/Biomedizinische Technik*. 2018;63:519–527.

How to cite this article: Freymüller C, Ströbl S, Aumiller M, Eisel M, Sroka R, Rühm A. Development of a microstructured tissue phantom with adaptable optical properties for use with microscopes and fluorescence lifetime imaging systems. *Lasers Surg Med*. 2022;54:1010–1026. <https://doi.org/10.1002/lsm.23556>